

Precision analysis of the photomultiplier response to ultra low signals

Pavel Degtiarenko*

Jefferson Lab, Newport News, Virginia, USA

Abstract

A new computational model for the description of the photon detector response functions measured in conditions of low light is presented, together with examples of the observed photomultiplier signal amplitude distributions, successfully described using the parameterized model equation. In extension to the previously known approximations, the new model describes the underlying discrete statistical behavior of the photoelectron cascade multiplication processes in photon detectors with complex non-uniform gain structure of the first dynode. Important features of the model include the ability to represent the true single-photoelectron spectra from different photomultipliers with a variety of parameterized shapes, reflecting the variability in the design and in the individual parameters of the detectors. The new software tool is available for evaluation of the detectors' performance, response, and efficiency parameters that may be used in various applications including the ultra low background experiments such as the searches for Dark Matter and rare decays, underground neutrino studies, optimizing operations of the Cherenkov light detectors, help in the detector selection procedures, and in the experiment simulations.

Keywords: Photon detector, Photomultiplier, Photoelectron, Signal amplitude spectra, Photon detection efficiency

1. Introduction

This work has been initiated by the new large-scale RICH detector [1] development undertaken as a part of the CLAS12 detector upgrade [2] at Jefferson Lab, during which a large number (more than 27 thousand) of the ultra low light detector channels needed to be studied, selected, and characterized. Solving this problem helped us to realize the importance of the new approach to a wider set of applications involving the multitude of the ultra low light detection systems.

The study revisits the problem of description and parameterization of the photomultiplier tube (PMT) response functions measured in the conditions of low light when only a few photoelectrons contribute to each measured signal. Correct evaluation of the single photoelectron (SPE) response is of significant interest for the photon detector science and metrology. It is also critical for many applications in the particle detector field where characterization of the detector response and efficiency is required for data analysis, and in astrophysics where precise photon flux measurements are vital, see, for example, Refs. [3, 4].

Several approaches to this problem have been developed and utilized, see Refs. [5, 6, 7, 8, 9, 10], and references therein. The common feature of the previous work in this field is the use of a rather rigid functional form for the description of the SPE spectra, such as the Poisson distribution form in [5, 6, 7, 8], the Gaussian form in [9], or a more complicated form of a weighted sum of Gaussian and exponential distribution in [10]. Certain types of photon detectors exhibit, however, more complicated

behavior of the spectra, see Refs. [11, 12, 13, 14, 15, 16]. Qualitatively it may be understood, for example, if the properties of the first amplification cascade of the device (the first dynode of a PMT) are non-uniform. This effect may be expected more visible in the multianode photomultiplier tubes (MAPMTs) in which the area along the edges of the first dynodes, possibly exhibiting different gain compared to the central parts, may be relatively large. Other physics effects and PMT design and construction features may contribute to the gain non-uniformity. SPE spectra in such cases can be expected to require a larger number of parameters for their description compared to the standard approach.

It is possible in principle to measure the SPE spectra experimentally at very low light conditions, and then use the data to predict the amplitude spectrum at any light [11]. The method is, however, resource consuming as the measurements at a really low light are difficult. Attempts to extract such detailed SPE spectra information from measurements in realistic conditions require complicated deconvolution algorithms [13].

This study presents a new method of describing the SPE spectra of virtually any reasonable complexity, therefore providing the tools for the understanding and characterization of the photon detector response in general. Finding a suitable structure of the SPE spectra and the set of parameters describing experimental signal amplitude distributions measured by the PMT photon detectors is the challenge that this work addresses. A systematic approach and successful solution to this problem opens better opportunities to characterize and calibrate such photon detectors, make an educated selection of sample devices that would work best for a particular purpose, create new software tools simulating behavior of the photon detectors

*Corresponding author Tel: +1 757 269 6274, Fax: +1 757 269 6050
Email address: pavel1@jlab.org (Pavel Degtiarenko)

in real installations.

2. General definitions

An amplitude response function of a photon detector in general, PMT in particular, may be defined in terms of probability distributions as described, for example, in Ref. [17]. Following the notation and terminology of [17], the function $f_{PMT}(s; parameters)$ represents the parameterized probability density function (p.d.f.) of signal amplitude (or charge) s .

The parameterized p.d.f. describes and may be used to approximate the probability distribution of the observed value of s in experiments in which multiple repeatable measurements are performed in stable conditions of constant low light delivered to the photon detector. A typical generalized setup for such measurements assumes that large and stable pulses of light are generated, short enough to be measured within the timing gates of the signal measurement system (and the gates in turn are selected as short as reasonably possible to minimize the noise contributions). The light pulse is then subjected to a heavy and stable filtering such that only a few photons per pulse reached the detector. Photons reaching the photon detector have a probability of knocking out the photoelectrons at the detector's first stage (photocathode in the case of a PMT), in accordance with its photoelectron emission efficiency. The number of the photoelectrons produced in one event is the integer random variable $m \geq 0$. The average number of photoelectrons in one event $\langle m \rangle \equiv \mu$ may be also defined as the ratio of the total number of photoelectrons generated to the number of triggers.

Every measurement in such setup is triggered externally, the resulting signal amplitude or charge is recorded, and thus the experimentally measured distribution is accumulated as a normalized function of s : $W(s) = (1/N_{tot})dN/ds$, where N_{tot} is the total number of triggers in the run, and dN/ds is the accumulated experimental histogram with bin width ds . Function $W(s)$ ($\equiv dN/ds$ p.d.f.) constitutes, therefore, the probability density function of observed value of s during the measurements.

Such normalized experimental distributions can be compared with $f_{PMT}(s; parameters)$, also normalized to unit area by definition. Then the set of parameters may be found, corresponding to the best description of the data by the parameterized function, using, for example, the method of maximum likelihood as described in [18].

The signal values s_{meas} are generally measured by a signal measurement system such as the Analog (or Charge) to Digital Converter (ADC, or QDC) devices, in units of their output (channels). The average pedestal value of the measured signal $\langle s_{ped} \rangle$ is obtained from the events with zero number of photoelectrons observed: $\langle s_{ped} \rangle \equiv \langle s_{meas} \rangle_{m=0}$. In a typical setup as described above, a noticeable portion of the events may produce no photoelectrons, satisfying the condition $m = 0$. The resulting measured random variable distribution on s_{meas} will exhibit corresponding peak at $s_{meas} = \langle s_{ped} \rangle$. The spread of the pedestal peak corresponds to the experimental resolution of the signal measurement system, and ideally is described by a Gaussian with the standard deviation σ (in channels). The pedestal

spread may be also measured in separate runs with the light source turned off, or the light completely filtered out.

The true signal value is defined here as

$$s = s_{meas} - \langle s_{ped} \rangle, \quad (1)$$

such that $\langle s \rangle_{m=0} = 0$ for events with $m = 0$. If $m > 0$, the average signal amplitude $\langle s \rangle$ is expected to be above zero. By definition, at $m = 1$ when only one photoelectron is produced, the s random variable will be distributed according to the SPE spectrum $p_1(s)$ p.d.f. Average s over the $p_1(s)$ p.d.f. spectrum defines the *scale* parameter, corresponding to the average signal value of the SPE signals:

$$scale = \langle s \rangle_{m=1}. \quad (2)$$

In linear systems the parameter *scale* is directly proportional to the value of the photon detector *gain*, that is, the ratio of the measured output current to the measured current from the photocathode.

Another convenient variable for use in the further discussion is the value of the normalized signal amplitude $a = s/scale$, such that $\langle a \rangle_{m=1} = 1$. The probability distribution of the a random variable, $f(a; parameters)$ p.d.f., can be linked to the $f_{PMT}(s; parameters)$ p.d.f. through the relation

$$f(a) = scale \cdot f_{PMT}(a \cdot scale; parameters), \quad (3)$$

to satisfy the normalization requirement

$$\int_{-\infty}^{\infty} f(a) da = 1. \quad (4)$$

The dependence on the vector of parameters is omitted for brevity in the $f(a)$ definition of Eq. (3), but assumed implicitly.

The probability distributions of the a random variable in the events with fixed number of photoelectrons $m \geq 0$ are defined as $p_m(a)$ p.d.f., with $p_0(a)$ characterizing the pedestal measurement, and $p_1(a)$ being the SPE spectrum, characteristic for the setup comprised of the photon detector and the signal measurement system.

The functions $p_m(a)$ are the result of the convolutions of the intrinsic photodetector response probability distribution functions $\rho_m(a)$ and the normalized signal measurement system resolution function $R(a)$ such that

$$p_m(a) = \int_{-\infty}^{\infty} dx R(x) \rho_m(a - x) \equiv \rho_m * R, \quad (5)$$

with $\rho_0(a) = \delta(a)$, and, correspondingly, $p_0(a) = R(a)$.

3. Photomultiplier response model

In the typical experimental setups as explained above, the random variable m is distributed according to the Binomial p.d.f. [17]. The two model assumptions of

- (a) stable and extremely small probability for an initial photon from the light source to pass the heavy filtering and knock out a photoelectron during one event, and
- (b) the absence of inter-dependency between the photoelectrons

– guarantee that the probabilities of observing m photoelectrons in one event will be distributed according to the Poisson distribution (see Refs. [11, 17]):

$$P(m; \mu) = \frac{\mu^m e^{-\mu}}{m!}. \quad (6)$$

The conditions (a) and (b) above, along with the model assumptions of

- (c) negligible noise contribution,
- (d) linearity of the signal measurement system, and
- (e) non-biased signal measurement system resolution function, corresponding to the condition $\langle R(a) \rangle = 0$

– allow us to unambiguously establish the relation between the value of the *scale* parameter, the average signal amplitude measured $\langle s \rangle$, and the average number of photoelectrons per one event μ :

$$scale = \langle s \rangle / \mu, \quad (7)$$

which follows from the property of the Poisson distribution to have its mean value equal to μ and the assumptions of independence, negligible noise, linearity, and non-biased measurement. Correspondingly, $\langle a \rangle = \mu$.

The five model assumptions (a) through (e), which seem to be realistic in many practical cases, are used in further discussions and model descriptions.

From these conditions it also follows that the intrinsic p.d.f. $\rho_2(a)$, being the distribution of the sum of two random variables each corresponding to the intrinsic SPE spectrum $\rho_1(a)$ p.d.f., can be explicitly expressed as their convolution

$$\rho_2(a) = \rho_1 * \rho_1 \equiv \rho_1^{*2}(a), \quad (8)$$

and, generally, for $m \geq 1$ photoelectrons the explicit expression

$$\rho_m(a) = \rho_1^{*m}(a) \quad (9)$$

is the convolution of m intrinsic SPE functions.

Thus, the p.d.f. for the intrinsic amplitude distribution from the photodetector becomes

$$\phi(a) = \sum_{m=0}^{\infty} P(m; \mu) \rho_m(a), \quad (10)$$

and the expression for the model p.d.f. $f(a)$ becomes

$$f(a) = \phi * R = e^{-\mu} R(a) + \sum_{m=1}^{\infty} P(m; \mu) \rho_1^{*m} * R. \quad (11)$$

The function $f(a)$ satisfies the normalization requirement (4) following the normalization of the Poisson p.d.f. and the normalization properties of the convolution algebra. A general

textbooks on Probability and Mathematical Statistics such as Refs. [19] and [20] may be consulted for the definitions and for the discussion of the convolution properties.

To find an appropriate functional form for the possible parameterization of the intrinsic function $\rho_1(a)$, we consider the process of electron multiplication at the second stage of the photodetector (at the first dynode of a PMT). Every photoelectron hitting the first dynode has a probability of knocking one or more second-stage electrons, which in turn will be amplified at the following dynodes. The average number of the second-stage electrons per one photoelectron, ν ($\equiv \nu_{\text{average}}$), can be considered a characteristic parameter of the detector. In every event, the number of the second-stage electrons n is a random variable which characterizes the eventually measured signal s . Thus, we may characterize the intrinsic SPE spectrum function $\rho_1(a)$ internally in the model by the discrete intrinsic probability distribution of the integer random variable n with its p.d.f. being the function of n : $q_1(n)$. Similarly, the discrete intrinsic functions $q_m(n)$ may be introduced, corresponding to the continuous intrinsic signal distributions $\rho_m(a)$.

We may also build the discrete intrinsic second stage amplitude distribution $\phi_2(n)$ similar to Eq. (10):

$$\phi_2(n) = \sum_{m=0}^{\infty} P(m; \mu) q_m(n) = e^{-\mu} q_0(n) + \sum_{m=1}^{\infty} P(m; \mu) q_1^{*m}(n), \quad (12)$$

where $q_0(n) = 0$ for all n , except $n = 0$, where $q_0(0) = 1$. The rules and properties of the convolutions of the discrete functions are similar to the convolutions of the continuous functions, with integration being replaced by summation.

The connection of the discrete intrinsic $\phi_2(n)$ p.d.f. to the continuous function $f(a)$ may be derived as follows. If we assume that the signal measurement system measures the number of second-stage electrons n directly, then the measured discrete signal distribution can be represented as a function of the normalized amplitude a in the form of the infinite sum of correspondingly weighted delta-functions, one per each value of $n \geq 0$:

$$D(a) = \sum_{n=0}^{\infty} \delta\left(a - \frac{n}{\nu}\right) \sum_{m=0}^{\infty} P(m; \mu) q_m(n), \quad (13)$$

where n in the argument of the delta-function is normalized to the average multiplicity ν of electrons produced by a single photoelectron at the first dynode, to provide the proper scale for the a variable, that is, to make average a to be equal to one in events with only one photoelectron.

The output of the signal measurement system, corresponding to the resulting model function $f(a)$, constitutes the convolution of the discrete intrinsic input spectrum of Eq. (13) with a realistic signal measurement resolution function $R(a)$ (often it is a Gaussian with the standard deviation parameter σ_a). The

convolution may be performed by integrating the equation

$$f(a) = \int_{-\infty}^{\infty} dx R(x) D(a-x) = \int_{-\infty}^{\infty} dx \frac{1}{\sqrt{2\pi} \sigma_a} \exp\left(-\frac{x^2}{2\sigma_a^2}\right) D(a-x). \quad (14)$$

The result of the integration may be presented in the form

$$f(a) = \sum_{n=0}^{\infty} G(a, n; \sigma_a) \sum_{m=0}^{\infty} P(m; \mu) q_m(n), \quad (15)$$

in which the probability of observing n electrons exiting the first dynode (the inner sum over m as defined in Eq. (12)) is multiplied by the function

$$G(a, n; \sigma_a) = \frac{1}{\sqrt{2\pi} \sigma_a} \exp\left[-\frac{(a - n/v)^2}{2\sigma_a^2}\right]. \quad (16)$$

The connection between the continuous and discrete intrinsic signal distributions for events at fixed m may be written correspondingly:

$$p_m(a) = \sum_{n=0}^{\infty} G(a, n; \sigma_a) q_m(n). \quad (17)$$

Eq. (15) with $G(a, n; \sigma_a)$ in the form of Eq. (16) corresponds to the model of a hypothetical photon detector consisting of only two stages of multiplication. For a PMT, it would be the photocathode and the first dynode. Such a device would be connected to a signal measurement system with a linear response and the Gaussian measurement function, measuring signals from any number of secondary electrons with the same resolution (standard deviation parameter of the Gaussian) σ in channels ADC. The standard deviation σ can be determined from the experimental data by fitting the pedestal amplitude distribution with a parameterized Gaussian, and the σ_a parameter in Eq. (16) would then be determined as

$$\sigma_a = \sigma / \text{scale}. \quad (18)$$

Realistic PMTs generally have more stages. The third one, and the stages that follow, may introduce extra statistical spread in the charge collected by the ADC at any given n . This can be modeled in the way similar to Eq. (12) by choosing the number of the third-stage electrons k as the integer random variable characterizing the signal s . The new discrete intrinsic third stage amplitude distribution $\phi_3(k)$ will look as follows:

$$\phi_3(k) = \sum_{m=0}^{\infty} P(m; \mu) \sum_{n=0}^{\infty} q_m(n) r_n(k), \quad (19)$$

where $r_n(k)$ is the p.d.f. for the probability of observing k electrons at the third stage of the PMT if the number of electrons at the second stage is n . Further stages can in principle be considered by building corresponding functions $\phi_4(l)$ (l being the

number of electrons at the fourth stage), etc. Practically, however, they would be of interest only if the signal measurement system was capable of resolving extremely small signals corresponding to a single electron from the corresponding stage. In this work we limit the model at the second stage, corresponding to the n random variable. Further stages help to define and model the additional statistical spread in conversion of the integer scale n into continuous scale s of the measured signal amplitude.

We approximate the extra statistical spread in the measured value of n , assuming there is another variable in the model, parameter ξ , corresponding roughly to the average number of the electrons knocked off at the third stage (from the second dynode of the PMT) by the electrons coming from the second stage (first dynode). The spread in the number of these third stage electrons is assumed to be purely statistical when the number of third-stage electrons is reasonably high ($n\xi > 10$), and is simulated using Eq. (19) otherwise, assuming that the gain at the fourth stage is equal to ξ also, and the statistical spread there is purely statistical. Such approximation cannot be used at a very small $\xi < 1$. In practice the PMT cascade multiplication factors at the second and third dynodes are generally well above 1.

The statistical spread is implemented in the model by substituting the σ_a parameter in Eq. (16) with the new parameter σ_{eff} which may depend on n ,

$$\sigma_{\text{eff}}(n) = \sqrt{\sigma_a^2 + \sigma_{\xi}^2} = \sqrt{\left(\frac{\sigma}{\text{scale}}\right)^2 + \frac{n}{v^2\xi}}, \quad (20)$$

which is the result of adding in quadrature the normalized sigma as defined in Eq. (18), and the parameterized spread of the measured amplitude by the third and further amplification stages of the detector. The relative statistical error for the value of the scaling term n/v in Eq. (16) is assumed to be

$$\frac{\sigma_{\xi}(n/v)}{n/v} = \frac{1}{\sqrt{n\xi}}. \quad (21)$$

Correspondingly, the quadrature contribution of this uncertainty to the overall standard deviation becomes

$$\sigma_{\xi}^2(n/v) = \frac{n}{v^2\xi}. \quad (22)$$

We note here that this approach will result in the pedestal peak in the spectrum (at $n = 0$) being described by the Gaussian with $\sigma_{\text{eff}}(0) = \sigma_a$. In experiments at low light where a significant portion of events results in no photoelectrons (corresponding to the values of $m = 0$ and $n = 0$), say, at μ less than 2-3, the pedestal peak can be used in the independent fit procedure to determine the value of σ .

So far we have introduced five parameters in the attempt to link the measured experimental signal amplitude distribution dN/ds p.d.f. and the parameterized function $f(a)$, namely, scale , σ , μ , v , and ξ . The problem will fully be solved when we find appropriate parameterized form for the function $q_1(n)$ for use in Eq. (12) such that the resulting parameterized function $f(a)$ of Eq. (15) could approximate experimental data successfully.

The simplest practical model for the production of the second-stage electrons is the model of independent Poissonian production with average ν , assuming that every photoelectron produces the secondary electrons independently and uniformly, as it was suggested in the earlier studies, see Refs. [5, 6, 7, 8]. The explicit form for the function $q_1(n)$ in such case is the Poisson distribution

$$q_1(n) = P(n; \nu) \equiv \frac{\nu^n e^{-\nu}}{n!}. \quad (23)$$

Rules for adding random Poissonian variables and convolution algebra (see, for example, Refs. [19, 20]) result also in the explicit form for the functions $q_m(n)$ at any $m \geq 1$:

$$q_m(n; \nu) = \frac{(m\nu)^n e^{-m\nu}}{n!} \equiv P(n; m\nu), \quad (24)$$

and the expression for the function $f(a)$ of Eq. (15) becomes the double sum on n and m :

$$f(a) = \sum_{n=0}^{\infty} \left\{ G(a, n; \sigma_{\text{eff}}) \left[e^{-\mu} q_0(n) + \sum_{m=1}^{\infty} P(m; \mu) P(n; m\nu) \right] \right\}. \quad (25)$$

For a given set of parameters and at any a the sum (25) may be evaluated numerically. Resulting function $f(a; \text{parameters})$ could be a reasonable approximation for the $dN/da(a)$ p.d.f. for some photodetectors. In the case of PMTs we have found that we need more flexibility and more than one parameter to describe the second-stage production function $q_1(n)$ satisfactorily.

Building on the above approach, we may increase the complexity and variability of the model approximation for the function $q_1(n)$ by assuming that several Poisson distributions with different averages can contribute to it. Qualitatively, such pattern could be observed, for example, in the case of a photomultiplier having a non-uniform first dynode with distinct areas of different first dynode gain. Generally, more parameters allow to investigate more complicated shapes of the function $q_1(n)$. Arguably, given enough gain components and corresponding extra free parameters, we could claim ultimately good description of any measured spectrum by decomposing it into a series of constituent Poisson distributions.

Assume that the discrete intrinsic SPE distribution function q_1 is composed of $L \geq 1$ elementary Poissonian components such that it can be presented in the form

$$q_1(n; \mathbf{v}_L) = \sum_{u=1}^L \alpha_u P(n; \nu_u), \quad (26)$$

wherein the corresponding partial gains, or average multiplicities of the Poissonian components are ν_1, \dots, ν_L , their relative contributions to the SPE function are $\alpha_1, \dots, \alpha_L$, satisfying the equation

$$\sum_{u=1}^L \alpha_u = 1, \quad (27)$$

and $\mathbf{v}_L = (\nu_1, \alpha_2, \nu_2, \dots, \alpha_L, \nu_L)$ is the vector of parameters, with $\mathbf{v}_1 \equiv (\nu_1)$, $\mathbf{v}_2 \equiv (\nu_1, \alpha_2, \nu_2)$, $\mathbf{v}_3 \equiv (\nu_1, \alpha_2, \nu_2, \alpha_3, \nu_3)$, etc.

In general, at any $m \geq 1$, $q_m(n; \mathbf{v}_L)$ may be written as

$$q_m(n; \mathbf{v}_L) = q_1^{*m}(n; \mathbf{v}_L) \equiv M_L(n, m; \mathbf{v}_L). \quad (28)$$

The equation for the multinomial $M_L(n, m; \mathbf{v}_L)$ function then follows from the properties of convolution powers (see Ref. [20]) applied to $q_1(n; \mathbf{v}_L)$:

$$\begin{aligned} M_L(n, m; \mathbf{v}_L) &= \left[\sum_{u=1}^L \alpha_u P(n; \nu_u) \right]^{*m} = \\ &= \sum_{\substack{i_1 + \dots + i_L = m \\ i_1, \dots, i_L \geq 0}} m! \prod_{u=1}^L \left(\frac{1}{i_u!} \alpha_u^{i_u} \right) P(n; \nu_{cL}), \end{aligned} \quad (29)$$

wherein

$$\nu_{cL} = \sum_{u=1}^L \nu_u i_u \quad (30)$$

is the average multiplicity of the secondary electrons in each of the (i_1, \dots, i_L) combinatorial elements contributing to the sum in Eq. (29). The combinatorial sum is performed for all L -dimensional combinatorial elements (i_1, \dots, i_L) satisfying the conditions $i_u \geq 0$ for each u , and $\sum_{u=1}^L i_u = m$. See Ref. [21] for the definitions and for the discussion of the multinomial coefficients in the sum.

The number L of elementary Poisson distributions in the decomposition of Eq. (26) can be chosen to accommodate expected or observed complexity in the SPE spectra. Larger L values would provide for more complicated spectral shapes, but require more computing resources, as well as increase the number of variable parameters, making the approximation process more difficult.

The explicit form for the function $M_1(n, m; \mathbf{v}_1)$ at $L = 1$ is similar to that of Eq. (24):

$$M_1(n, m; \mathbf{v}_1) = P(n; \nu_1 m), \quad (31)$$

at $L = 2$ it can be represented as the binomial sum:

$$\begin{aligned} M_2(n, m; \mathbf{v}_2) &\equiv B(n, m; \mathbf{b}) = \\ &= \sum_{i=0}^m \frac{m!}{i!(m-i)!} (1 - \alpha_2)^i (\alpha_2)^{m-i} P(n; \nu_1 i + \nu_2 m - \nu_2 i), \end{aligned} \quad (32)$$

and at $L = 3$ it corresponds to the trinomial sum:

$$\begin{aligned} M_3(n, m; \mathbf{v}_3) &\equiv \\ &\equiv T(n, m; \mathbf{t}) = \sum_{\substack{i_1 + i_2 + i_3 = m \\ i_1, i_2, i_3 \geq 0}} \frac{m!}{i_1! i_2! i_3!} \alpha_1^{i_1} \alpha_2^{i_2} \alpha_3^{i_3} P(n; \nu_c), \end{aligned} \quad (33)$$

wherein

$$\nu_c = \nu_1 i_1 + \nu_2 i_2 + \nu_3 i_3 \quad (34)$$

is the average multiplicity of the secondary electrons in each of the (i_1, i_2, i_3) combinatorial elements, and

$$P(n; \nu_c) = \frac{(\nu_c)^n \exp(-\nu_c)}{n!}. \quad (35)$$

Table 1: List of PMT model fit parameters

Name	Limits	Brief Description
$scale$	> 0	average amplitude of SPE signals (channels ADC)
σ	> 0	standard deviation of the pedestal fit (channels ADC)
μ	> 0	average multiplicity of photoelectrons
ν_1	> 0	average multiplicity of the first gain component in (26)
α_2	$[0, 1]$	portion of second gain component in (26)
ν_2/ν_1	$[0, 1]$	relative multiplicity of the second gain component in (26)
$\alpha_3/(1 - \alpha_2)$	$[0, 1]$	relative portion of third gain component in (26)
ν_3/ν_1	$[0, 1]$	relative multiplicity of the third gain component in (26)
ξ	> 1	average multiplicity at the second dynode

The trinomial sum of Eq. (33) proved to be sufficient in characterizing the measured SPE amplitude distributions in this study.

Thus, for the purpose of the approximation of the amplitude distributions experimentally measured in PMT photon detectors we use the following equation:

$$f(a; \mathbf{d}) = \sum_{n=0}^{\infty} \left\{ G(a, n; \sigma_{\text{eff}}) \left[e^{-\mu} q_0(n) + \sum_{m=1}^{\infty} P(m; \mu) T(n, m; \mathbf{t}) \right] \right\}. \quad (36)$$

The set of parameters \mathbf{d} includes $scale$, σ , μ , ξ , and the vector $\mathbf{t} = (\nu_1, \alpha_2, \nu_2, \alpha_3, \nu_3)$. The average multiplicity of the secondary electrons produced by one photoelectron (average second stage gain) in this case will be

$$\nu = \nu_1(1 - \alpha_2 - \alpha_3) + \nu_2\alpha_2 + \nu_3\alpha_3. \quad (37)$$

The list of parameters taking full advantage of the PMT spectra approximation by Eq. (36) is given in Table 1. Parameter forms ν_2/ν_1 , $\alpha_3/(1 - \alpha_2)$, and ν_3/ν_1 are used in the computations to simplify the fit procedure as the limits on these parameter forms can be set universally. The original equation's symmetry between parameters ν_1, ν_2 , and ν_3 , and between α_1, α_2 , and α_3 is broken in the fitting procedure to make it more stable. The model parameters may be extracted from their table forms unambiguously.

4. Implementation of the model

The fitting procedure was written in KUIP [22] macro language and in FORTRAN within the framework of the Physics Analysis Workstation (PAW) [23] package from CERN, with the use of the multiparametric functional minimization routine

MINUIT [24]. The software development tools chosen are a bit outdated. However, the choice of KUIP as the high-level programming language, operating effectively with the data analysis objects, both interactively and in the batch mode, helped significantly in the relatively quick development of the fit algorithm and procedure. The FORTRAN code for the fitting function and the KUIP macro language routines with the implementation examples are available upon request. Currently, plans to export the code into the Root [25] environment are under consideration.

Numerical evaluation of the function $f(a; \mathbf{d})$ in Eq. (36) is performed by setting finite limits of summation over n and m . The upper limit on m in this study, at relatively low average photoelectron multiplicities $\mu \lesssim 3$, is set at 16. The contribution of higher values of m to the sum is negligible at such conditions. The limits of summation over n are selected dependent on the value of a such that $|a - n/\nu| < 8\sigma_{\text{eff}}$, neglecting the value of the Gaussian $G(a, n; \sigma_{\text{eff}})$ of Eq. (16) beyond 8 standard deviations. If the lower limit obtained from the above condition is below zero, it is set at $n = 0$. The values of the model limiting parameters can be adjusted if needed for different conditions, for example, higher values of μ may require using higher upper limit on m .

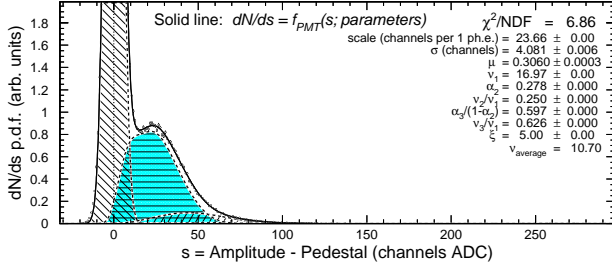
No formal proof of the convergence of the summation method has been developed; however, an indirect verification is done every time by checking that the calculated function is normalized to unit area in accordance with Eq. (4), with accuracy much better than 1%.

As an independent verification of the implementation of the method, we observe that the mean a value for the $p_m(a)$ p.d.f. calculated using Eq. (17) is $\langle a \rangle = m$ as expected for all $m \geq 0$.

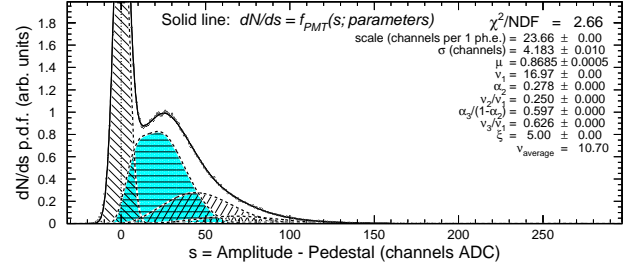
In the fitting procedure, a raw measured amplitude distribution dN/ds is normalized to have the integral (the sum of all channels in the histogram) to be equal to one, representing the measured probability distribution dN/ds p.d.f., to be approximated by the model probability density function $f_{PMT}(s; \mathbf{d})$. The first guess of the values of $\langle s_{\text{ped}} \rangle$ and σ is made based on the Gaussian fit of the left side and top of the first peak in the distribution, representing events with $n = 0$. The average amplitude $\langle s \rangle$ is then calculated together with the initial estimate of μ parameter to obtain the initial value of the $scale$ parameter, which allows us to present the probability distribution as a function of normalized signal amplitude a . After that, the data set is used in the process of finding the best set of parameters describing it in the form of Eq. (36), using MINUIT.

The stability of the multiparametric fitting procedure strongly depends on the right choice of the parameters' initial values. In the following examples, different strategies were implemented to achieve such stability, generally by splitting the process into several stages, starting with the separate fit of the pedestal Gaussian to determine the pedestal position and standard deviation, then setting the initial value of μ by evaluating the portion of events in the pedestal region and using the assumption that it is equal to $\exp(-\mu)$, and then gradually increasing the number of variable parameters in the consequent fits.

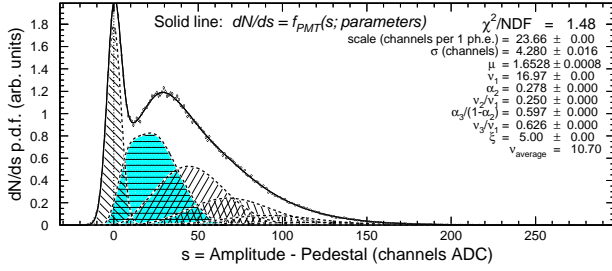
In the examples that included measurements of amplitude



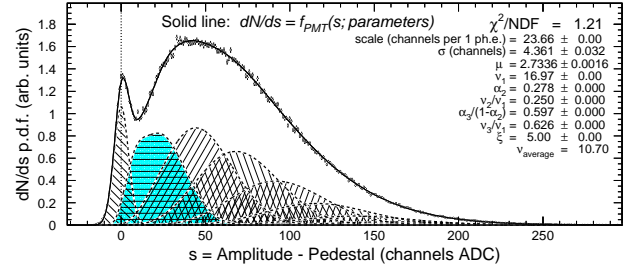
(a) H8500 MAPMT, anode #39, test setup at low light conditions corresponding to $\mu = 0.306$



(b) H8500 MAPMT, anode #39, test setup at lower-medium light conditions corresponding to $\mu = 0.869$



(c) H8500 MAPMT, anode #39, test setup at upper-medium light conditions corresponding to $\mu = 1.653$



(d) H8500 MAPMT, anode #39, test setup at higher light conditions corresponding to $\mu = 2.734$

Figure 1: A set of amplitude distributions measured with a Hamamatsu H8500 photomultiplier, anode #39, at ten light conditions, four of which are shown. The experimental data [27] are shown as open circles with error bars, the fit function $f_{PMT}(s; parameters)$ is shown as a solid line, and the contributions to f_{PMT} coming from events with zero, one, and more photoelectrons are shown as areas under dashed lines with different types of hatch. The area corresponding to the SPE contribution uses horizontal lines as hatch type, and is highlighted. Only two parameters, σ and μ , are left variable in all final fits.

distributions from the same photodetector in identical conditions, only varying the amount of light delivered to the detector per one measurement, the procedure included the next layer of a “global fit”. After the best set of parameters describing each individual measurement was found, the parameters related to the SPE amplitude distribution were averaged across the set and fixed at those values. The remaining “external” parameters (such as $scale$, μ , and σ) were set free for the subsequent fit. The cycle of fitting procedures starting with releasing all the parameters and making a new fit, averaging the SPE parameters and fixing them at the new values, and then re-fitting only “external” parameters was performed several times until final convergence was reached. The quality of the resulting approximation is an indication that the parameters of the SPE distribution were found correctly and may serve as values characterizing the device. These data sets illustrate the “predictive power” of the model, that is, its ability to predict how the amplitude distributions would look in different experiments with the same PMT (at different light conditions, and with different resolution of the signal measurement, for example).

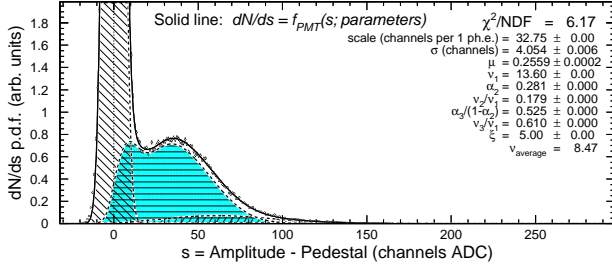
5. Examples

This section provides examples of practical applications of the model used for parameterizations of real signal amplitude spectra measured in various conditions and with different types of photomultipliers.

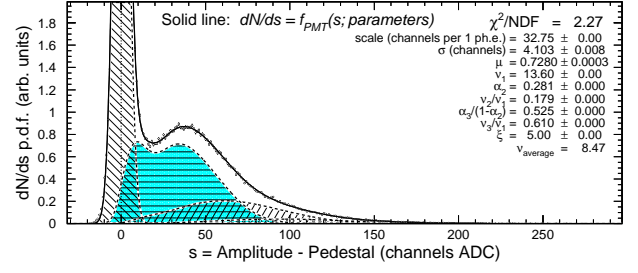
5.1. Tests of Hamamatsu H8500C-03 Multianode PMT

Figures 1, 2, and 3 illustrate the general quality of the model description of the amplitude distributions measured on three different anodes of the position sensitive Hamamatsu MAPMT H8500C-03, a 52 mm square 12-stage photomultiplier tube with 64 (matrix 8 by 8) pixels [26]. The measurement was a part of the dedicated study of the SPE detection capabilities of this PMT and its performance in a high magnetic field [27]. The spectra from each anode were accumulated in several irradiation conditions, corresponding to the range of μ from about 0.3 to 3. The raw data sets were kindly presented to us by the Authors of Ref. [27] for the analysis. Every spectrum was subjected to the two-level “global fit” procedure as described in the previous section. The fitting function is visibly following the data points nicely above the pedestal. The values of χ^2/NDF , or χ^2/n_d as per [18], corresponding to the formal goodness-of-fit statistical evaluators, are mostly determined by the quality of the Gaussian approximation for the signal measurement system resolution function in this experiment. At low-light setups, where the pedestal events dominate, the non-Gaussian contributions to the shape of the resolution functions increase the values of χ^2/n_d , but do not disturb significantly the SPE spectra parameterizations in this example.

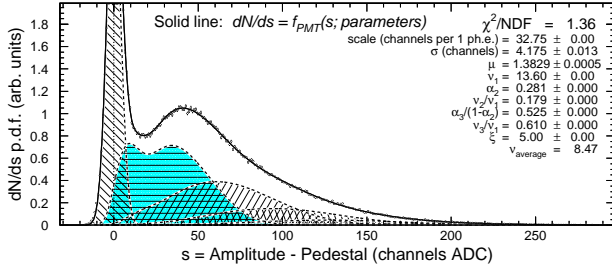
We found that the best-fit parameters of the SPE amplitude distributions, while different for different anodes, are close within statistical errors for different irradiation conditions of one pixel (anode) of the PMT. The data are described well in different light setups with the same fixed set of parameters v_1 ,



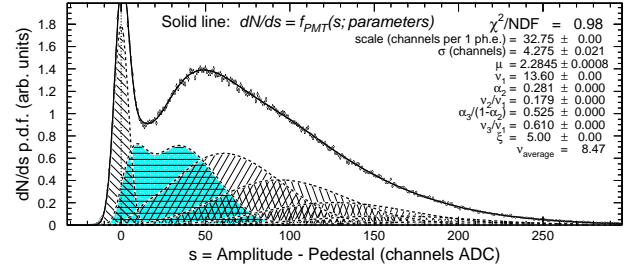
(a) H8500 MAPMT, anode #45, test setup at low light conditions corresponding to $\mu = 0.256$



(b) H8500 MAPMT, anode #45, test setup at lower-medium light conditions corresponding to $\mu = 0.728$

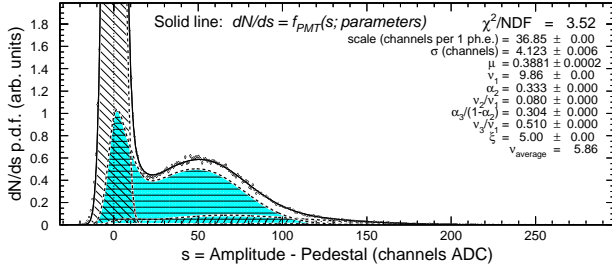


(c) H8500 MAPMT, anode #45, test setup at upper-medium light conditions corresponding to $\mu = 1.383$

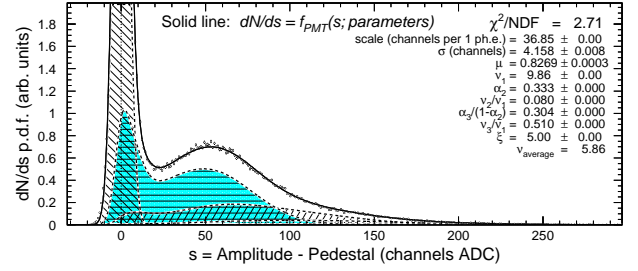


(d) H8500 MAPMT, anode #45, test setup at higher light conditions corresponding to $\mu = 2.285$

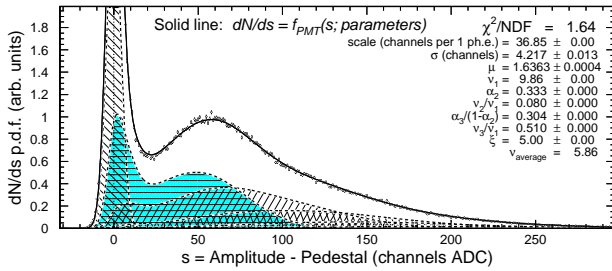
Figure 2: A set of amplitude distributions measured with a Hamamatsu H8500 photomultiplier, similar to the set shown in Fig. 1, but on different anode #45. Ten measured distributions participated in the “global fit” procedure; four of them are shown.



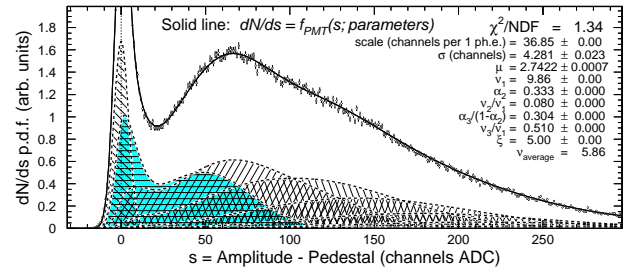
(a) H8500 MAPMT, anode #61, test setup at low light conditions corresponding to $\mu = 0.388$



(b) H8500 MAPMT, anode #61, test setup at lower-medium light conditions corresponding to $\mu = 0.827$



(c) H8500 MAPMT, anode #61, test setup at upper-medium light conditions corresponding to $\mu = 1.636$

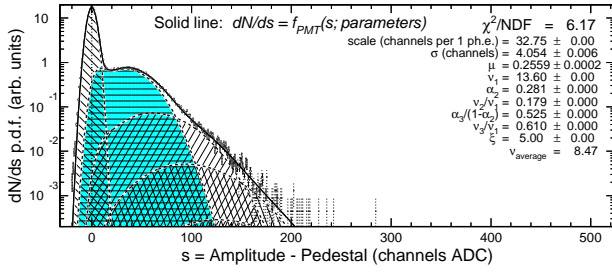


(d) H8500 MAPMT, anode #61, test setup at higher light conditions corresponding to $\mu = 2.742$

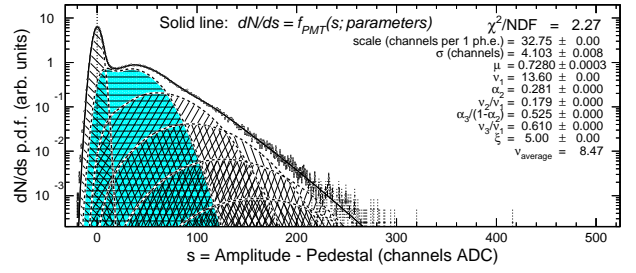
Figure 3: A set of amplitude distributions measured with a Hamamatsu H8500 photomultiplier, similar to the set shown in Fig. 1, but on different anode #61. Nine measured distributions participated in the “global fit” procedure; four of them are shown.

α_2 , v_2 , α_3 , v_3 , ξ of the SPE spectrum $p_1(a)$, keeping variable only the parameter specifying the light (μ), and one of the signal measurement parameters, σ . The values of the fixed parameters

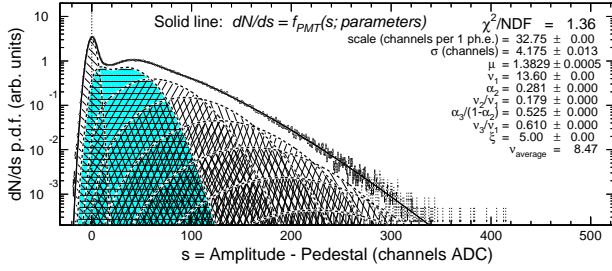
are shown in the plots with zero standard deviations. The data sets allowed us also to keep the $scale$ parameter fixed in all fits, indicating to a good stability of the signal measurement sys-



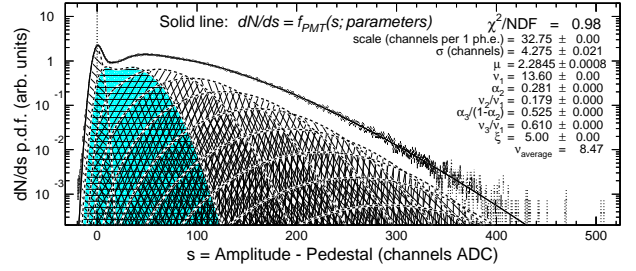
(a) H8500 MAPMT, anode #45, test setup at low light conditions corresponding to $\mu = 0.256$



(b) H8500 MAPMT, anode #45, test setup at lower-medium light conditions corresponding to $\mu = 0.728$



(c) H8500 MAPMT, anode #45, test setup at upper-medium light conditions corresponding to $\mu = 1.383$



(d) H8500 MAPMT, anode #45, test setup at higher light conditions corresponding to $\mu = 2.285$

Figure 4: Same as in Fig. 2, but using logarithmic scale in ordinate to illustrate the contribution of higher m components in the spectra.

tem during the measurements. To illustrate these observations better, the plots are normalized such that the SPE contribution to the full spectra is shown (as the dashed line above the highlighted and horizontally hatched area) visually identical in each plot of the set. The SPE spectrum approximation extracted from the data in such a procedure may therefore be considered as a characteristic of the photon detector (one of the anodes of the MAPMT in this case).

This result demonstrates the predictive functionality of the model, meaning that the SPE spectrum approximation measured in some conditions may be used to evaluate the amplitude distributions from this detector in different light conditions, and with different signal measurement resolution.

Logarithmic scales in ordinate in Fig. 4 illustrate the quality of the model description of the whole spectra as the sum of the partial terms with m from 0 to about 7-10.

5.2. Tests of ET Enterprises 9823B PMT

Fig. 5 shows similar exercise with the amplitude spectra measured on a very different PMT, ET Enterprises 5-inch 9823B tube; the data were kindly provided to us by Hakob Voskanyan, Andrey Kim and Will Phelps [28]. The statistical errors in the data set are small enough for a stable and accurate multiparametric fitting procedure. The excellent quality of the data made it possible to observe and measure the non-Gaussian components in the pedestal distributions, and adjust the model by introducing and parameterizing these components of the experimental signal measurement distribution function, to achieve acceptable model description of the full data set.

We did observe the slight asymmetry in the pedestal function that could be modeled by introducing an exponential noise component in addition to the standard Gaussian form. Such noise may be modeled *ad hoc* as an independent random value a_{noise} contributing with a certain probability to the signal value a in any event, and distributed according to the exponential

$$f_{\text{noise}}(a; \tau) = \frac{1}{\tau} \exp\left(-\frac{a}{\tau}\right), \quad (38)$$

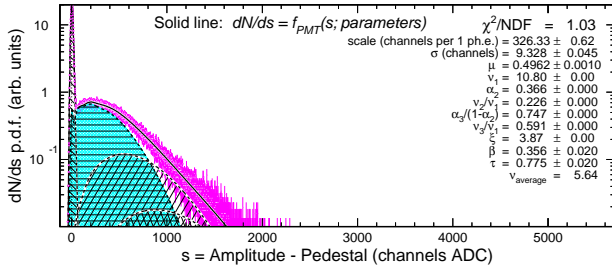
with the parameter τ describing the exponential (temperature-like) noise spectrum.

Adding such a random noise contribution to the model involves the convolution between the model function (36) and the exponential (38). Using the properties of the convolution algebra, it can be implemented by the substitution of the Gaussian form $G(a, n; \sigma_{\text{eff}})$ in Eq. (36) with its convolution with the exponential noise in the form

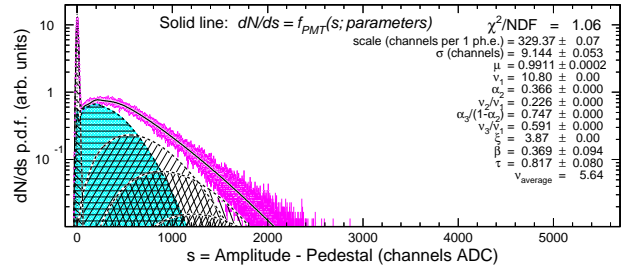
$$(1 - \beta)G(a, n; \sigma_{\text{eff}}) + \beta G_{em}(a, n; \sigma_{\text{eff}}, \tau), \quad (39)$$

wherein the parameter β is the probability for the noise event to happen in every measurement, and the function $G_{em}(a, n; \sigma_{\text{eff}}, \tau)$ is the convolution of the Gaussian with the exponential (known also as exponentially modified Gaussian distribution, see Ref. [29]):

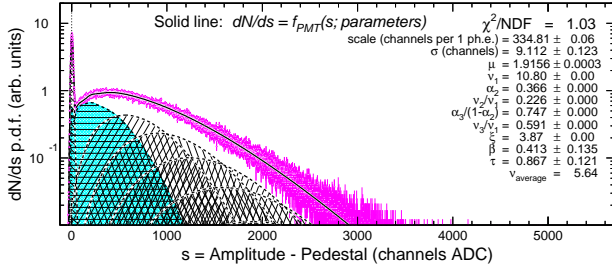
$$G_{em}(a, n; \sigma_{\text{eff}}, \tau) = \frac{1}{2\tau} \exp\left(\frac{\sigma_{\text{eff}}^2}{2\tau^2} - \frac{a - n/\nu}{\tau}\right) \cdot \text{erfc}\left[\frac{\sigma_{\text{eff}}^2/\tau - (a - n/\nu)}{\sqrt{2}\sigma_{\text{eff}}}\right], \quad (40)$$



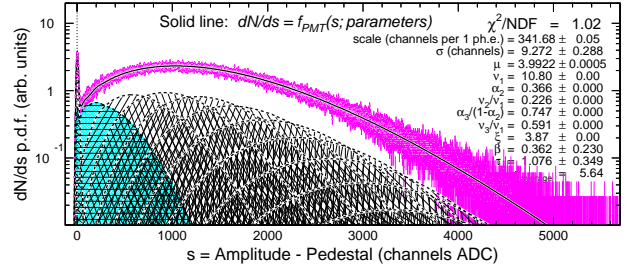
(a) ET Enterprises 9823B PMT, test setup at low light conditions corresponding to $\mu = 0.496$



(b) ET Enterprises 9823B PMT, test setup at lower-medium light conditions corresponding to $\mu = 0.991$



(c) ET Enterprises 9823B PMT, test setup at upper-medium light conditions corresponding to $\mu = 1.916$



(d) ET Enterprises 9823B PMT, test setup at higher light conditions corresponding to $\mu = 3.992$

Figure 5: A set of amplitude distributions measured with an ET Enterprises 9823B photomultiplier at eighteen light conditions, four of which are shown. The experimental data [28] are shown as open circles with error bars, other notation and the features in the plots are the same as in Fig. 1. The values of τ parameter in the plots are dimensionless and given in the units of σ . Only the parameters related to the performance of the signal analysis system ($scale$, σ , β , and τ), and also the light intensity parameter μ are left variable in the final fits.

where

$$\text{erfc}(x) \equiv 1 - \text{erf}(x) = \frac{2}{\sqrt{\pi}} \int_x^\infty \exp(-t^2) dt. \quad (41)$$

Adding random exponential noise contributions to every measurement in this extension of the model eliminates the property of the system resolution function $R(a)$ to be non-biased, violating the basic assumption (e) in the model. The correspondingly modified relation of Eq. (7) between the values of the $scale$, $\langle s \rangle$, and μ parameters that should be applied in the minimization procedure in this case is as follows:

$$scale_{\beta\tau} = (\langle s \rangle - \beta\tau)/\mu. \quad (42)$$

The results of application of such approach to the data are illustrated in Fig. 5. The set of 18 measurements at different light intensities in the range of μ values from about 0.5 to about 4.0 was approximated using the identical SPE spectrum defined by the parameters v_1 , α_2 , v_2 , α_3 , v_3 and ξ . The signal measurement system parameters $scale$, σ , β and τ were left variable in the global fit procedure to allow for their slight modification between different measurements, but their variations are quite small, showing the stability of the test setup. The only major variable parameter in the fitting procedure is μ , characterizing average number of photoelectrons in each test. The goodness-of-fit evaluator χ^2/n_d is in the range between 1.0 and 1.1 in all 18 approximations, indicating to a model description of the data close to a theoretically perfect.

5.3. Extracted SPE spectra

Fig. 6 further illustrates the inner structure of the SPE spectra extracted from the data sets shown in Figs. 1-3 and Fig. 5. The $p_1(a)$ p.d.f. are drawn as functions of the normalized signal amplitude a , together with their three Poissonian components defined by the vectors of parameters \mathbf{t} . The $p_1(a)$ functions are shown convoluted with the corresponding effective signal measurement Gaussians $G(a, n; \sigma_{\text{eff}})$ in Figs. 6a-6c, and convoluted with the modified signal measurement function of Eq. (39) in Fig. 6d. The parameters for the signal measurement functions used were averaged over the test light conditions.

The three components of the $p_1(a)$ functions originate from the three elementary Poissonian constituents of the discrete $q_1(n)$ distributions, as defined in Eq. (26), and are converted to the continuous a scale by the same convolutions applied to each component separately, similar to how it's done in Eq. (17). The components add up to fit the complicated SPE amplitude distribution functions that would be difficult to approximate using a smaller number of parameters.

Good normalized signal amplitude resolution of the measurement system for the data shown in Fig. 6d allowed us to clearly distinguish between the events with $n = 0$ and events with $n > 0$ in the SPE spectrum, that is, to evaluate according to the model the portion of events when a photoelectron fails to generate any response from the PMT. Portion of such events in the $p_1(a)$ function may be linked to the "collection efficiency" characteristic reported by the PMT manufacturers, see, for example, Ref. [16], page 45.

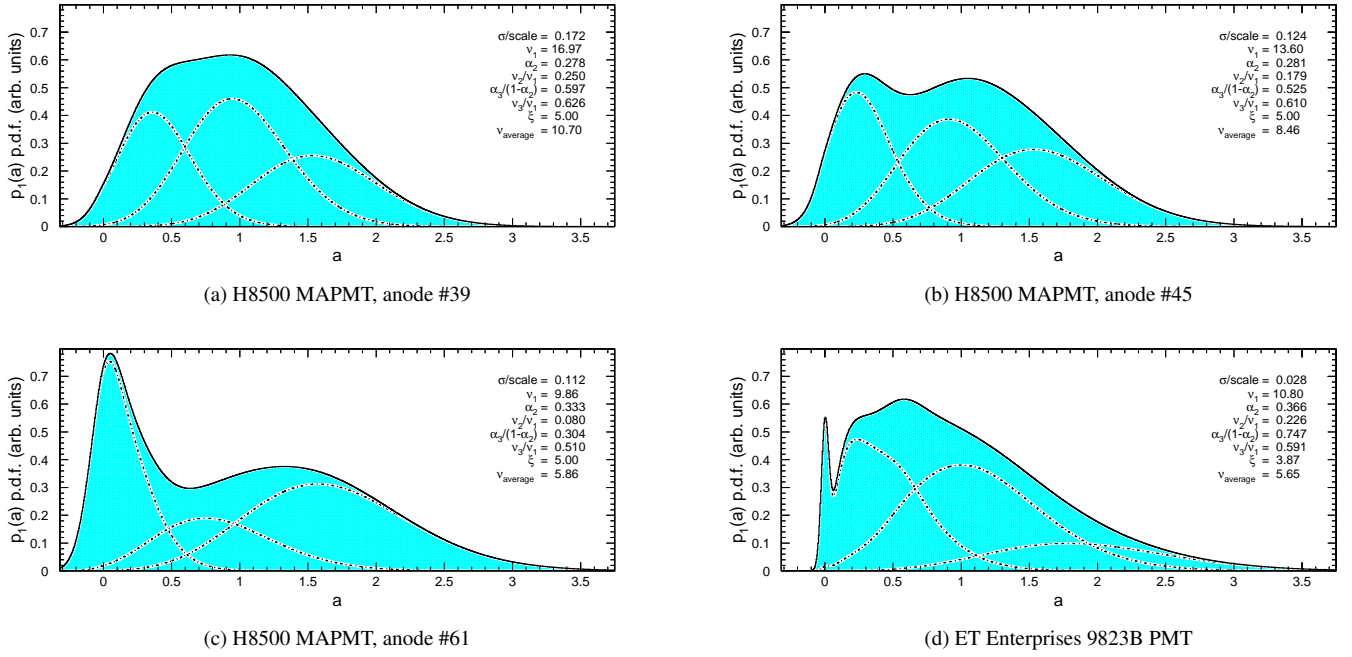


Figure 6: Solid lines show the $p_1(a)$ p.d.f. corresponding to the amplitude spectra of a single photoelectron as determined in the plots shown in Figs. 1-3 (panels a-c), and Fig. 5 (panel d). The trinomial components of the functions are shown by the dash-dotted lines.

5.4. Tests of Hamamatsu H8500 and H12700 MAPMTs

The following example illustrates some of the results of the study of large number (430) of the Hamamatsu H8500 and H12700 MAPMTs, obtained in the process of PMT selection for the new RICH detector, which is presently underway at JLab [1, 30]. As opposed to H8500, the new 10-stage H12700 series of MAPMTs from Hamamatsu [26] is designed specifically to suit better for the applications requiring reliable single photoelectron detection, such as RICH detectors.

All the MAPMTs were tested in the conditions of a relatively low light (three illumination conditions identified as “OD54”, “OD50” and “OD46”, corresponding to the parameters of average μ of about 0.06, 0.13, and 0.20, and at four values (1000, 1050, 1075 and 1100 volts) of the operational high voltage (HV) applied.

The total number of measured amplitude distributions recorded and analyzed is about 340 thousand. The signal measurement system did not provide perfect Gaussian pedestal amplitude distributions during these tests. While the pedestal shapes were very close to Gaussian form, the small statistical errors in the peak made the fitting procedure very sensitive to the small distortions, and thus unstable. To avoid parameterization instabilities caused by the discrepancies between the ideal Gaussian pedestal shape and the measured pedestal peaks, in every spectrum the statistical errors in the data points constituting the pedestal peaks were increased and re-normalized such that the peaks could be approximated by the Gaussian functions with the new modified $(\chi^2/n_d)_{\text{Gaussian}}$ equal to one. That way during the multiparameter fitting procedure the disturbed pedestal peak shapes did not influence the main χ^2 of the full spectrum minimization. Essentially only pedestal position and

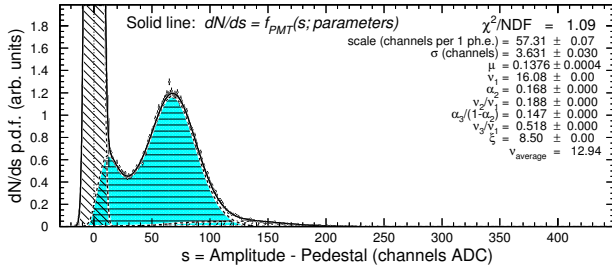
effective Gaussian width were used in the main fitting procedure, not details of the shape.

The parameters of the SPE spectrum for each of the 27,520 anodes were obtained using the “global fit” procedure. The SPE parameters were averaged over the runs with different illumination conditions and fixed in final fits.

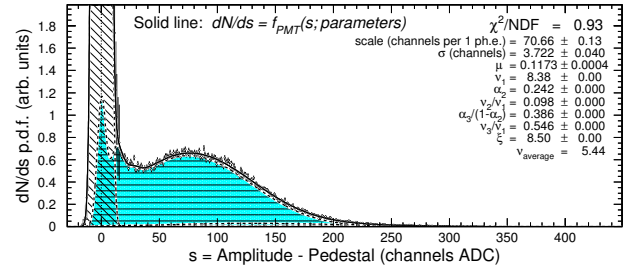
Fig. 7 shows the characteristic examples of the spectra measured on one of the central anodes belonging to a MAPMT H12700 (left panels) and to a MAPMT H8500 (right panels) at four different applied high voltages from 1000 V to 1100 V, together with the model approximations.

Each plot shows the quality of the overall fit of the data by the model function, mostly defined by the SPE contribution at such low-light test conditions. The significant increase of the *scale* parameter with the increase of the applied high voltage may be seen clearly, corresponding to the well-known dependence of PMT gains on the applied high voltage. Notice that the extracted values of μ parameter are quite stable and practically do not depend on HV. The H12700 MAPMTs generally exhibit a more prominent high- ν component of the SPE spectrum compared with the H8500 tubes.

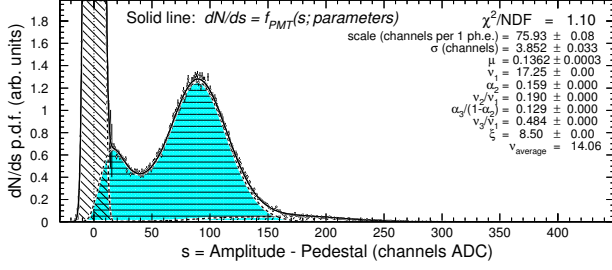
The model-approximated SPE spectra measured for several anodes of the sample MAPMTs, including those corresponding to the set of plots from Fig. 7, are shown in Fig. 8, function of the normalized amplitude a . Despite the strong dependence of the *scale* parameter on the applied high voltage observed earlier, the shapes of the SPE spectra function of a are stable and only slightly depend on the HV, possibly due to the changes in the average multiplicity ν of the second-stage electrons knocked from the first dynode. Qualitatively this result may be understood such that as energy of the photoelectron ac-



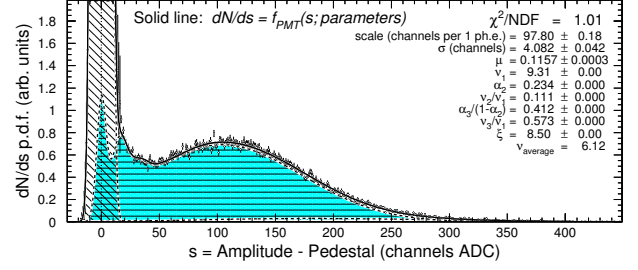
(a) Hamamatsu H12700 MAPMT GA0133, HV = 1000 V



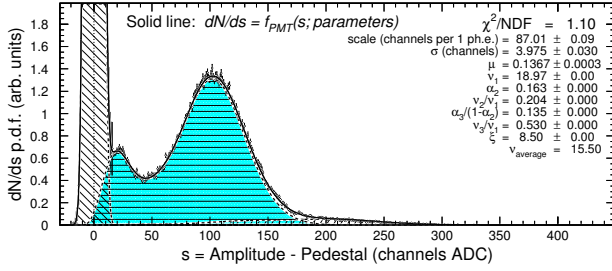
(b) Hamamatsu H8500 MAPMT CA7782, HV = 1000 V



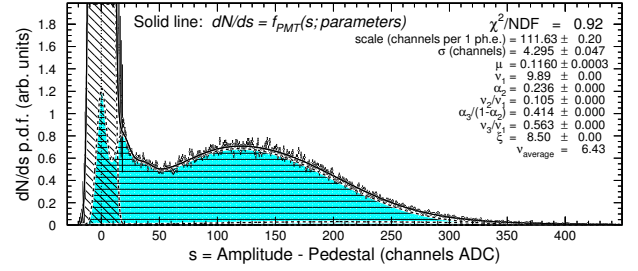
(c) Hamamatsu H12700 MAPMT GA0133, HV = 1050 V



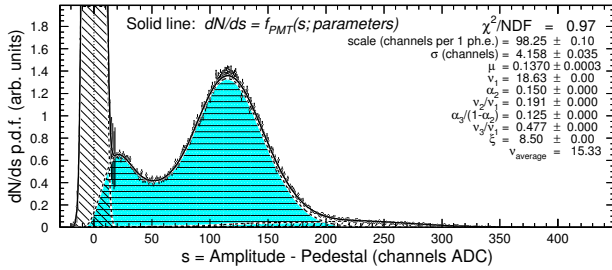
(d) Hamamatsu H8500 MAPMT CA7782, HV = 1050 V



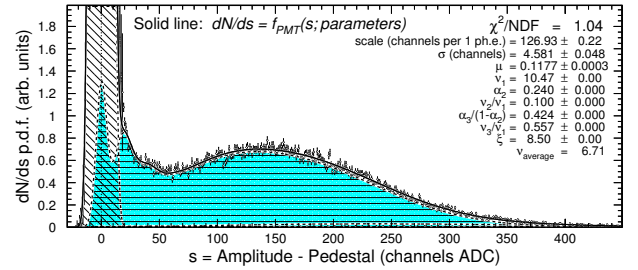
(e) Hamamatsu H12700 MAPMT GA0133, HV = 1075 V



(f) Hamamatsu H8500 MAPMT CA7782, HV = 1075 V



(g) Hamamatsu H12700 MAPMT GA0133, HV = 1100 V



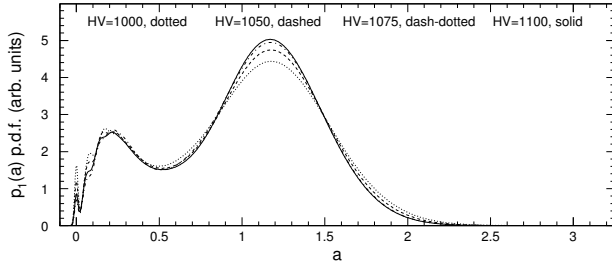
(h) Hamamatsu H8500 MAPMT CA7782, HV = 1100 V

Figure 7: A set of amplitude distributions measured at four high voltages on one Hamamatsu H12700 MAPMT (left panels), and one Hamamatsu H8500 MAPMT (right panels), shown for one of the central anodes (#28) in each MAPMT at the medium “OD50” light condition. The notation and other features in the plots are the same as in Fig. 1. Only the set of parameters related to the performance of the signal analysis system ($scale$ and σ), and also the light intensity parameter μ are left variable in the final fits.

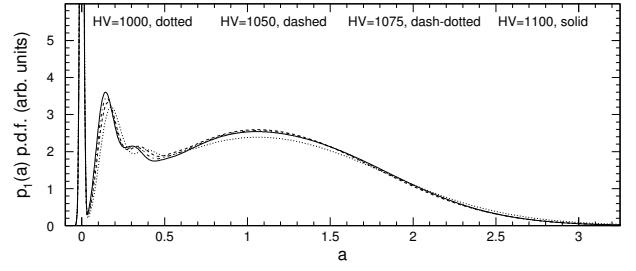
celeration from the photocathode to the first dynode increases at higher voltages, the average number of the knocked-out electrons increases slightly. Such pattern is observed in all anodes and all photomultipliers in the study.

The variability of the SPE parameters between different anodes in each MAPMT is found to be quite significant. Also significant is the difference between average SPE parameters for H8500 and H12700 MAPMT types. Fig. 9 illustrates this

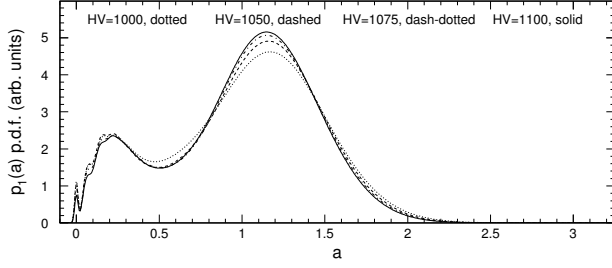
statement by showing some of the “PMT Passport” plots for the above two MAPMT example devices. Model approximation parameters were obtained for every anode independently using the “global fit” procedure, and plotted as a function of the anode number for every photomultiplier. Model parameters $scale$, μ , and the derived values of $v_{average}$ and ε on the left panels in Fig. 9 are obtained for the H12700 example MAPMT, and corresponding right panels show the results for the H8500



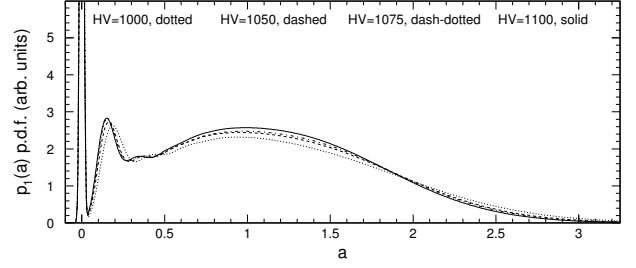
(a) Hamamatsu H12700 MAPMT GA0133, anode #28



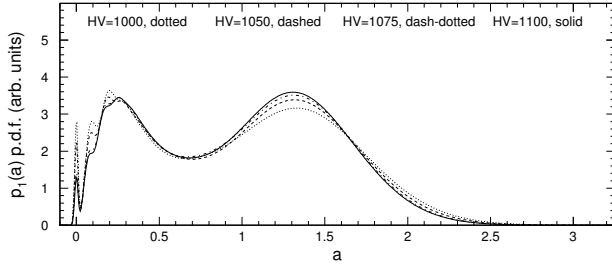
(b) Hamamatsu H8500 MAPMT CA7782, anode #28



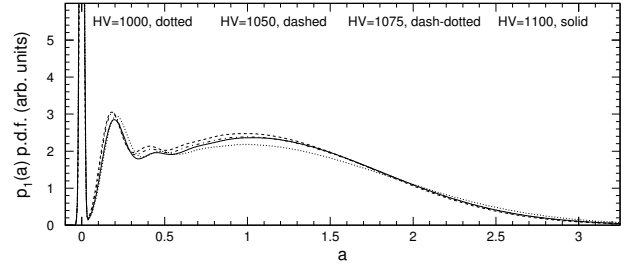
(c) Hamamatsu H12700 MAPMT GA0133, anode #32



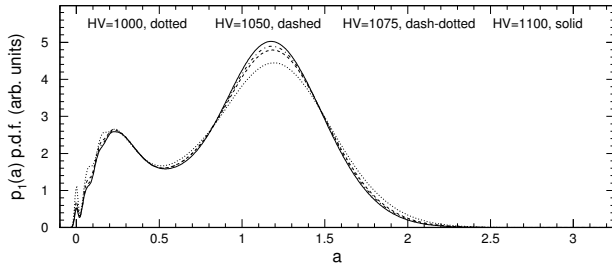
(d) Hamamatsu H8500 MAPMT CA7782, anode #32



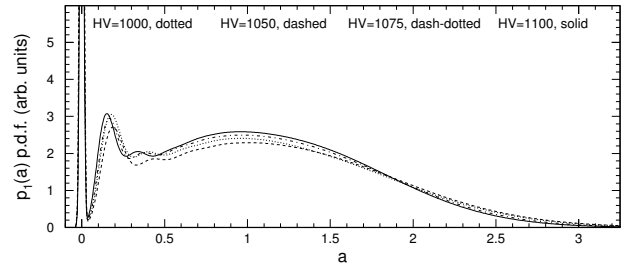
(e) Hamamatsu H12700 MAPMT GA0133, anode #57



(f) Hamamatsu H8500 MAPMT CA7782, anode #57



(g) Hamamatsu H12700 MAPMT GA0133, anode #64



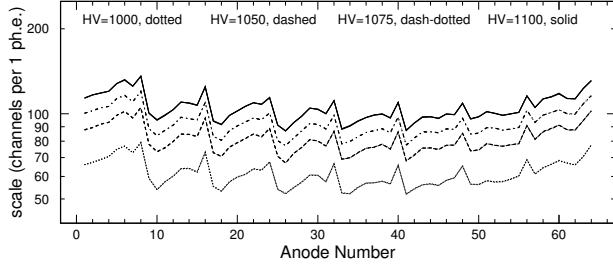
(h) Hamamatsu H8500 MAPMT CA7782, anode #64

Figure 8: Each panel shows the SPE p.d.f., measured using the “global fit” procedure at four high voltage values. Four anodes are shown for both types of MAPMTs, corresponding to the anode positions at the center, at the center of the edge, and at the two corners of the MAPMT’s face. All plots show the $p_1(a)$ p.d.f. assuming artificially small normalized experimental measurement resolution $\sigma/scale = 0.02$.

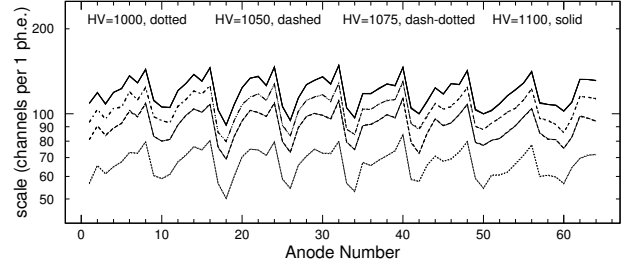
MAPMT. The SPE efficiency evaluation parameter ε will be discussed further in the text.

The top panels (a) and (b) in Fig. 9 illustrate typical variable patterns of the $scale$ parameters as a function of anode number. The plots show all twelve test conditions that the MAPMTs were subjected to in this study, namely, four HV values times three light conditions. Quite striking feature of the model approximation is that the extracted $scale$ parameters do not depend on the light conditions to a very high degree of accuracy,

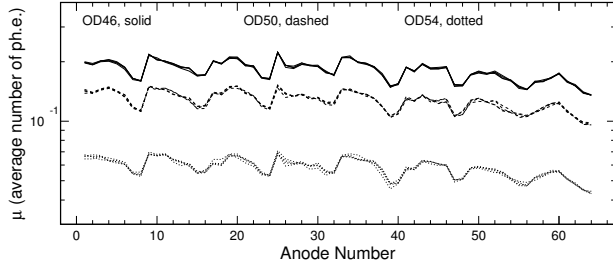
such that those differences practically cannot be resolved on the plots. The dependence of the $scale$ parameter on HV is on the other hand quite clear and corresponds to the well-known characteristic exponential dependence of output amplitudes (PMT gain) on high voltage. The data sets, measured at different high voltages and plotted as a function of the anode number, look essentially parallel in logarithmic scale in the plots, meaning that their difference may be approximately attributed to multiplication by a factor.



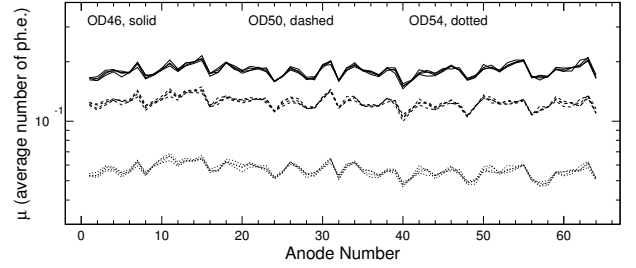
(a) Parameter $scale$, proportional to the overall PMT gain at each anode. H12700 MAPMT “GA0133”



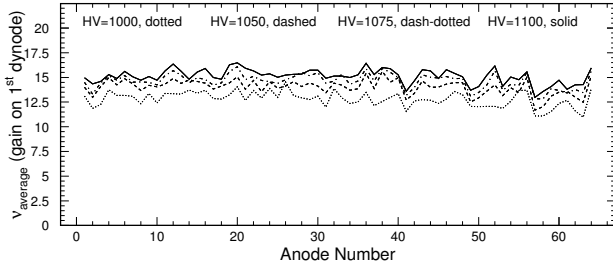
(b) Same as in (a), but for the H8500 MAPMT “CA7782”



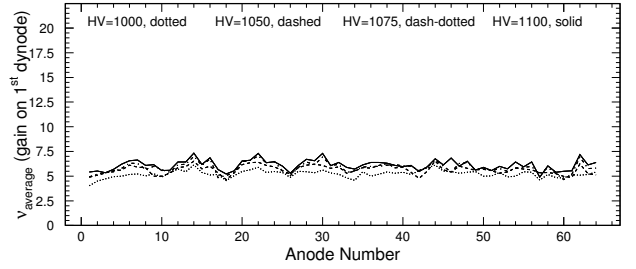
(c) Parameter μ , proportional to the light intensity at each anode. H12700 MAPMT “GA0133”



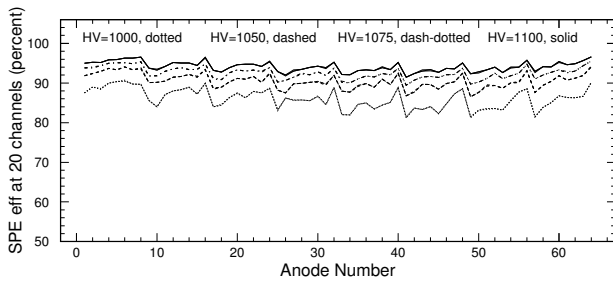
(d) Same as in (c), but for the H8500 MAPMT “CA7782”



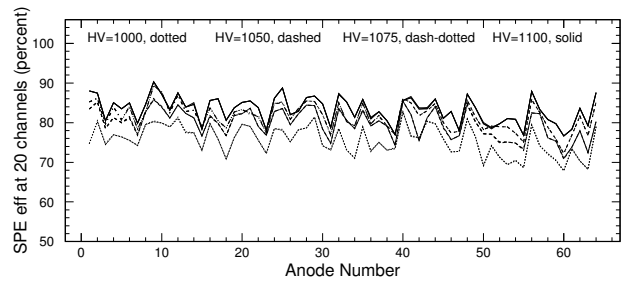
(e) Average number of the second-stage electrons knocked out by one photoelectron, for each anode. H12700 MAPMT “GA0133”



(f) Same as in (e), but for the H8500 MAPMT “CA7782”



(g) Efficiency ε of one photoelectron detection at each anode. H12700 MAPMT “GA0133”



(h) Same as in (g), but for the H8500 MAPMT “CA7782”

Figure 9: MAPMT passport plots: a selection of the model parameters $scale$, μ , and the derived values of ν and ε , evaluated using the “global fit” procedure for the two sample devices, Hamamatsu H12700 MAPMT “GA0133” (left panels), and H8500 MAPMT “CA7782” (right panels), plotted as functions of the anode numbers of these MAPMTs. All twelve data sets are shown in each plot, corresponding to the three illumination conditions measured at each of four different applied high voltages.

Panels (c) and (d) in Fig. 9 are complementary to the previous two in a sense that they show the stability of the model

in determining the model parameter μ during the varying test conditions. Naturally μ must be proportional to the average

light delivered during the test, and ideally it wouldn't depend on the HV applied. These regularities are generally observed in the data. As the irradiation of the MAPMT face was uniform, μ measured in each of the 64 channels change in sync with changing light conditions. The dependence of the μ parameter on the high voltage applied is very minimal, and possibly could be explained by such effects as the tiny increase in the probability of photoelectron emission in higher gradients of electric fields in the photocathode region, or by better focusing of the photoelectrons at higher voltages. However, these hypotheses weren't further investigated in this work.

Panels (e) and (f) in Fig. 9 show the ν derived value as defined in Eq. (37), function of the anode number for the sample MAPMTs. The values of ν are averaged over the three light conditions at each of the HV settings using the “global fit” procedure. The difference in ν values between the H12700 and H8500 MAPMT models is quite significant and is observed in other MAPMTs through the whole data set. Most likely explanation of this observation is the difference in the design of these MAPMTs. Other typical feature that could be seen in these two panels is the relatively weak, but noticeable, dependence of ν on the high voltage applied. Such dependence of ν on HV may be qualitatively understood as increasing probability of knocking out electrons from the first dynode at higher voltages due to higher energy that a photoelectron acquires when accelerating from the photocathode to the first dynode.

Panels (g) and (h) in Fig. 9 illustrate one of the possible final goals of such studies: evaluate efficiency ε of the photoelectron detection by the photodetectors. Here ε is defined as the probability of events distributed according to the evaluated SPE amplitude distributions $p_1(s)$ to have their signal amplitude s above 20 channels ADC or QDC as recorded by the signal measurement system during these tests. The value of ε generally varies from anode to anode, as shown in the plots in correlation with the anode gain, which in turn depends on the high voltage applied. The efficiency is systematically higher for the H12700 MAPMT series, despite generally higher *scale* parameters observed for the H8500 MAPMTs.

The overall features of the massive analyzed MAPMT data set are presented in the following plots.

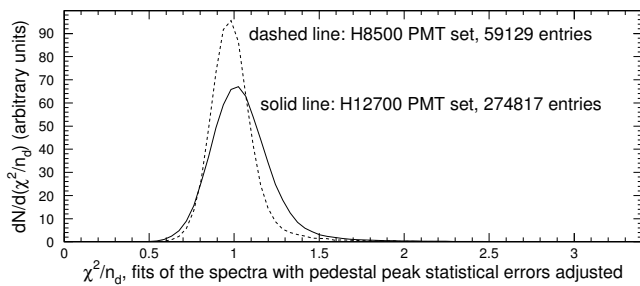


Figure 10: Distribution of the goodness-of-the-fit evaluator χ^2/n_d on the number of model parameterizations. Dashed line shows the H8500 set, solid line - the set of fits for the H12700 MAPMTs. The distributions are normalized to equal areas in the plot.

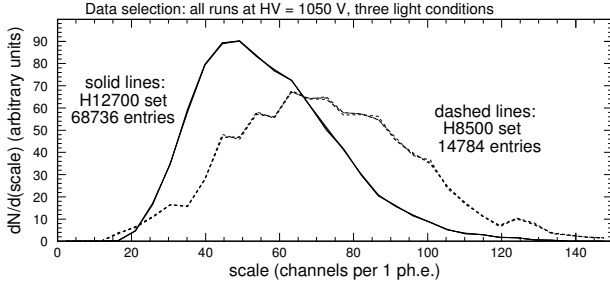
Fig. 10 shows the distributions of the goodness-of-fit eval-

uator χ^2/n_d for about 60000 parameterizations for the H8500 MAPMTs in this study, and about 275000 parameterizations for the H12700 MAPMT series. The χ^2/n_d value is taken from the last stage of the “global fit” procedure in which the six parameters characterizing the SPE spectra were averaged and fixed for the 3 setups at different light conditions, and other variables were optimized to minimize the χ^2 . As it was explained above, the values of statistical errors in the bins around the pedestal in the raw spectra were artificially adjusted to make the fit insensitive to the slightly non-Gaussian shape of the measured peak and avoid fit instabilities. The χ^2/n_d distributions are normalized to equal areas under the curves. While both distributions indicate to a reasonably good quality of the fits, the H8500 series is closer to being “theoretically perfect”, and the H12700 series distribution has more instances of the fits with a somewhat less than perfect quality.

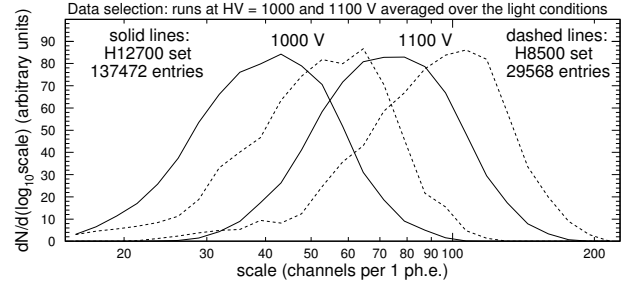
Fig. 11 presents distributions of *scale* and μ model parameters, and the derived values of ν and $\mu\varepsilon$ for the analyzed data sets. Dashed lines show the H8500, and solid lines the set of parameters for the H12700 MAPMTs. The distributions are normalized to equal areas in the plots. The selections of the parameter sets included in the distributions are indicated on top of the panels.

Fig. 11a shows the distributions of *scale* parameter measured for all anodes of H8500 and H12700 MAPMTs at 1050 V. As it has already been illustrated in the panels (a) and (b) of Fig. 9, the extracted *scale* parameters do not depend on the light conditions to a very high degree of accuracy. The distributions of the *scale* parameter in Fig. 11a accumulated for the different light conditions are practically identical and are superimposed on top of each other in the plot. While the spread of the values is quite broad, the H8500 set exhibits *scale* values on average about 20% larger than the H12700 set at the same HV. Apparently, as compared to the H8500 MAPMT, the lower number of the amplification stages in the H12700 devices is almost compensated by the new design features allowing greater amplification at each stage. This is further illustrated in Fig. 11b where the *scale* parameter distributions are shown for HV = 1000 V and HV = 1100 V, averaged over the light conditions, and plotted using the logarithmic scale in abscissa to better see the similarities between the distributions at different applied voltages.

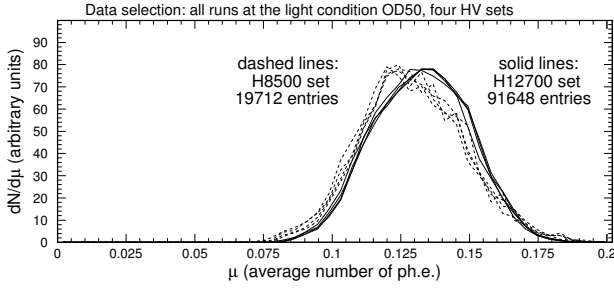
Fig. 11c shows the distributions of μ parameter measured for all anodes of H8500 and H12700 MAPMTs at the intermediate light condition “OD50”, and all high voltages. The distributions indicate on a rather small (< 10%) difference in the photoefficiency and/or photoelectron collection ability between the two types of MAPMT, showing the slight advantage for the H12700 devices. It may also be seen in the plot, that the evaluated parameters μ practically do not depend on HV applied. This observation illustrates the good level of factorization between the *scale* and μ parameters of the model. The values of these parameters evaluated in one set of the test conditions are applicable to the tests at different HV and light. While the stability of the extracted *scale* parameter is observed to be within the small statistical errors of under 1%, the distributions on μ may indicate on the presence of a slight (1-2%) dependence of μ on the applied HV. However, this small effect was difficult to evalu-



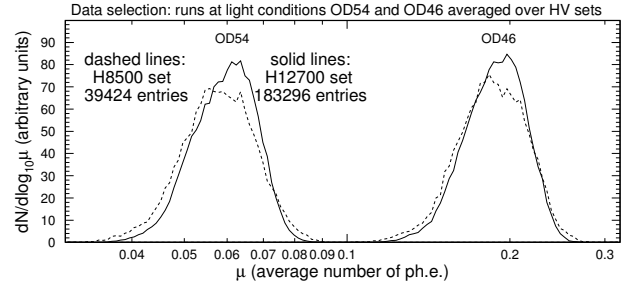
(a) Distributions of $scale$ parameter for the two MAPMT data sets



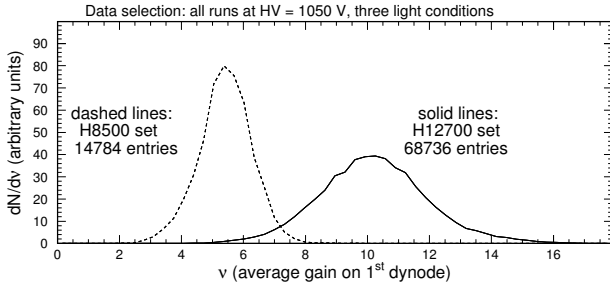
(b) Light-averaged distributions of $scale$ parameter for the two MAPMT data sets, in the two HV settings



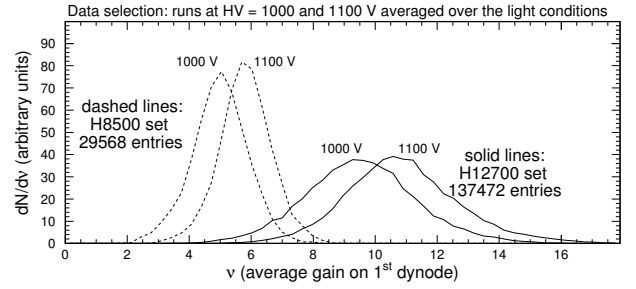
(c) Distributions of μ parameter for the two MAPMT data sets



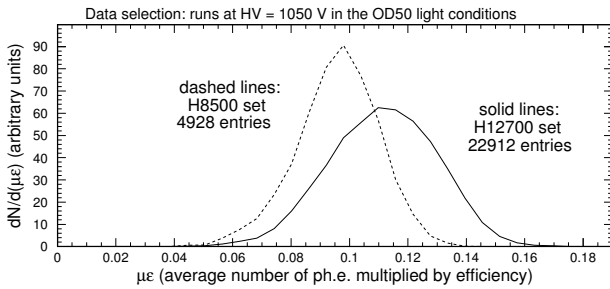
(d) HV-averaged distributions of μ parameter for the two MAPMT data sets, in the two light conditions



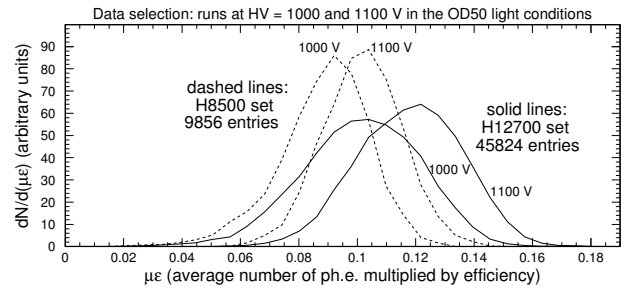
(e) Distributions of ν value for the two MAPMT data sets



(f) Light-averaged distributions of ν value for the two MAPMT data sets, in the two HV settings



(g) Distributions of the light detection efficiency value $\mu\epsilon$ for the two MAPMT data sets at HV = 1050 V



(h) Same as (g) for the HV settings at 1000 V and 1100 V

Figure 11: Distributions of $scale$ and μ parameters, and ν and $\mu\epsilon$ derived values on the number of model parameterizations. Dashed lines show the H8500 data set, and solid lines the set of parameters for the H12700 MAPMTs. The distributions are normalized to equal areas in each plot. The selections of the evaluated parameter sets included in the distributions are indicated on top of the panels.

ate and analyze in more detail. Averaging over the sets of tests at different HV allowed us to further illustrate the differences between the H8500 and H12700 data in the distributions on μ

measured at different light conditions, presented in Fig. 11d.

Fig. 11, panels (e) and (f) are similar to panels (a) and (b) in the same figure, but showing the derived value of the ν param-

ter for the same sets of conditions. According to the model, the set of the SPE parameters of the photon detector do not depend on the light conditions during the tests. This condition is taken into account during the “global fit” procedure, leading to the ν independence of the light conditions. Thus, Figs. 11(e,f) illustrate the difference of the derived ν values between the H8500 and H12700 MAPMTs, and also its dependence on the HV applied. While the HV-dependence is relatively weak, the difference between the two types of MAPMTs is quite dramatic, indicating that the average number of the second-stage electrons knocked out of the first dynode is almost twice as large in a H12700 MAPMT compared to H8500 in the same conditions.

Panels (g) and (h) in Fig. 11 illustrate the comparison between the H8500 and H12700 sets of MAPMTs in terms of their ultimate efficiencies of detecting light. At the same signal thresholds in channels ADC, H12700 MAPMTs have some advantage in the probability of detecting light, in spite of generally smaller SPE signals (the $scale$ parameter). The advantage is due to a somewhat larger photon conversion efficiency (the μ parameter), and better shapes of the SPE spectra with much larger ν value for H12700 devices, corresponding also to a better collection efficiency for them.

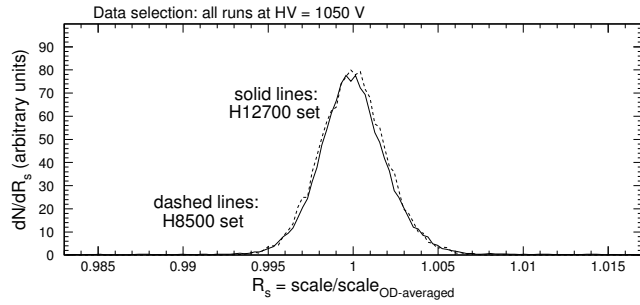


Figure 12: Distributions of the stability evaluator for the $scale$ parameter, corresponding to the relative statistical error in the extracted value of the $scale$ for the two MAPMT data sets. See text for details.

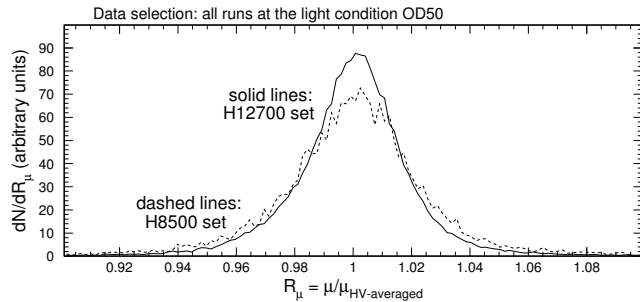


Figure 13: Distributions of the stability evaluator for the μ parameter, corresponding to the combination of the relative statistical error in the extracted value of the μ , and the observed weak dependence of μ on the applied HV, for the two MAPMT data sets. See text for details.

Fig. 12 and Fig. 13 illustrate the levels of relative stability achieved in the evaluation of the major SPE parameters $scale$ and μ , by plotting the ratios of individually evaluated parameters to the values of the same parameters averaged over the

measurements in different conditions, in which the model ideally should give the same values ($scale$ measured in the three light conditions in the case of Fig. 12, and μ measured at four values of applied HV in the case of Fig. 13). While the distribution of the stability evaluator for the $scale$ parameter $R_s = scale/\langle scale \rangle_{OD-averaged}$ is indeed ultimately good (the spread is about 0.5% FWHM), the corresponding spread in the distribution of $R_\mu = \mu/\langle \mu \rangle_{HV-averaged}$ is about 4% FWHM. The latter observation may indicate, apart from the statistical differences between the parameters, to an additional weak dependence of the average number of photoelectrons μ on the applied high voltage.

The extracted SPE characteristics for each anode in the whole studied set of multianode photomultipliers were stored in a general MAPMT parameter database. The accumulated data will facilitate and improve the detector selection process, and will help to model the detector response and efficiency. The SPE spectral functions extracted in such analysis may serve as objective internal characteristics of each photon detector (each anode of a MAPMT in this case) at an abstract level, independent of the test conditions. For an extended experimental setup, the set of such functions describing each detector may be used to evaluate overall detector performance in current working conditions that could be different from the test environment.

6. Conclusion

The new computational model for description of the photomultiplier response functions has been developed, implemented, and tested in real applications. Important features of the model include the ability to approximate the true single-photoelectron spectra from different photomultiplier tubes with a variety of parameterized spectral shapes, reflecting the variability in the design and in the individual parameters of the detectors. The new techniques were developed in the process of building the model, such as the method of decomposition of the SPE spectra into a series of elementary Poisson probability density functions, and the use of convolution algebra to build the multi-photoelectron amplitude distributions describing measured spectra.

The “predictive power” of the model has been tested by demonstrating that the SPE spectral parameters, obtained in the real measurements, may describe well the amplitude distributions measured at different levels of irradiation of the same photodetector. Thus, the model allowed us to extract the characteristic parameters of the devices independently of the test measurement conditions. In that way the set of parameters obtained in one or several test runs at certain running conditions could serve to obtain predicted detector response and efficiency for a wider set of running conditions, for a varying level of light during the real runs, and/or for a different amplitude resolution of the measurement system.

The SPE spectral parameterization information in experimental physics or industrial photon detector setups may be utilized to make an educated selection of the devices that would work best for a particular purpose, make choices for the characteristics of the readout electronics necessary for a particular

setup, and create new software tools simulating expected behavior of the photon detectors in real installations for use in the data analysis procedures.

Acknowledgements

This material is based upon work supported by the U.S. Department of Energy, Office of Science, Office of Nuclear Physics under contract DE-AC05-06OR23177. The author thanks Alex Vlassov, Valery Kubarovsky, and Bogdan Wojtsekhowski for their stimulating interest in the work and useful suggestions. The work wouldn't be possible without the data sets accumulated by different experimental groups and kindly presented to me for analysis by their Authors: Valery Kubarovsky, Andrey Kim, Simona Malace, Brad Sawatzky, Hakob Voskanyan, Youri Sharabian, Will Phelps and Rachel Montgomery.

REFERENCES

References

- [1] M. Contalbrigo et al., "The large-area hybrid-optics CLAS12 RICH detector: Tests of innovative components", Nucl. Instrum. and Meth. **A 766** (2014) p. 22.
- [2] CLAS Collaboration at Jefferson Lab, "CLAS12 Technical Design Report", version 5.1 (2008), p. 208.
- [3] M. Vicić et al., "Fast pulsed UV light source and calibration of non-linear photomultiplier response", Nucl. Instr. and Meth. **A 507** (2003), p. 636.
- [4] C. Blaksley and P. Gorodetzky, "A setup for the precision measurement of multianode photomultiplier efficiency", Nucl. Instr. and Meth. **A 764** (2014), p. 198.
- [5] F.J. Lombard and F. Martin, "Statistics of Electron Multiplication", Rev. Sci. Instr. **32** (1961) 200.
- [6] H.J. Gale and J.A.B. Gibson, "Methods of calculating the pulse height distribution at the output of a scintillation counter", J. Sci. Instr. **43** (1966) 224.
- [7] J. Rademacker, "An exact formula to describe the amplification process in a photomultiplier tube", Nucl. Instr. and Meth. **A 484** (2002) 432.
- [8] I. Chirikov-Zorin, I. Fedorko, A. Menzione, M. Pikna, I. Sykora, S. Tokar, "Method for precise analysis of the metal package photomultiplier single photoelectron spectra", Nucl. Instr. and Meth. **A 456** (2001), p. 310.
- [9] E.H. Bellamy et al., "Absolute calibration and monitoring of a spectrometric channel using a photomultiplier", Nucl. Instr. and Meth. **A 339** (1994), p. 468.
- [10] R. Dossi, A. Ianni, G. Ranucci, and O.Ju. Smirnov, "Methods for precise photoelectron counting with photomultipliers", Nucl. Instr. and Meth. **A 451** (2000), p. 623.
- [11] A.G. Wright, "A Monte Carlo simulation of photomultiplier resolution", IEEE Transactions on Nuclear Science, **NS-34**, No. 1 (1987), p. 414.
- [12] B. Wojtsekhowski, private communication.
- [13] M. Shepherd and A. Pope, "Investigation of BURLE 8854 Photomultiplier Tube", JLab Technical Note TN97-028 (1997).
- [14] J. McCann, "Finding the average number of photoelectrons in an ADC charge spectrum", JLab internal publication, (1998).
- [15] "Photomultiplier Tubes - Principles and Applications", Re-edited September 2002 by S.O. Flyckt and C. Marmonier, Photonis, Brive, France, Chapter 2, p. 8.
- [16] "Photomultiplier Tubes - Basics and Applications" Third Edition (Edition 3a), August 2007 by Hamamatsu Photonics K.K. Editorial Committee, Chapter 6, p. 128.
- [17] K.A. Olive et al. (Particle Data Group), "Review of Particle Physics", Chin. Phys. C **38**, No. 9 (2014) 090001, Chapter 37 (Probability), p. 467. See also online version at <http://pdg.lbl.gov/2014/reviews/rpp2014-rev-probability.pdf>, last accessed on March 27, 2017.
- [18] Ibid., Chapter 38 (Statistics), p. 472. See also online version at <http://pdg.lbl.gov/2014/reviews/rpp2014-rev-statistics.pdf>, last accessed on March 27, 2017.
- [19] G. Grimmett and D. Welsh, "Probability: An Introduction", Second Edition, Oxford University Press (2014), Chapter 3.4, p. 72. For a quick reference see also https://proofwiki.org/wiki/Sum_of_Independent_Poisson_Random_Variables_is_Poisson, last accessed on March 27, 2017.
- [20] Hogg, Robert V.; McKean, Joseph W.; Craig, Allen T. "Introduction to mathematical statistics" (6th ed.). Upper Saddle River, New Jersey: Prentice Hall (2004). For a quick reference see also http://en.wikipedia.org/wiki/Convolution_power and http://en.wikipedia.org/wiki/Convolution#Algebraic_properties, both sites last accessed on March 27, 2017.
- [21] "NIST Handbook of Mathematical Functions", Editors F.W.J. Olver, D.W. Lozier, R.F. Boisvert, C.W. Clark, University of Maryland and National Institute of Standards and Technology, Maryland (May 2010), Chapter 26.4. See also <http://dlmf.nist.gov/26.4>, last accessed on March 27, 2017.
- [22] R. Brun, et al., "KUIP - Kit for a User Interface Package", Program Library I102, CERN, Geneva, Switzerland (1993).
- [23] R. Brun, O. Couet, C. Vandoni, and P. Zanarini, "PAW users guide", Program Library Q121, CERN, Geneva, Switzerland (1991).
- [24] F. James, "MINUIT - Function minimization and error analysis", Reference Manual, Program Library D506, CERN, Geneva, Switzerland (1998).
- [25] R. Brun and F. Rademakers, "ROOT - An Object Oriented Data Analysis Framework", Nucl. Inst. and Meth. **A 389** (1997) 81-86. See also <http://root.cern.ch/>, last accessed on March 27, 2017.
- [26] HAMAMATSU PHOTONICS K.K. See <http://www.hamamatsu.com/>, or http://www.hamamatsu.com/resources/pdf/etd/PMT_TPMZ0002E.pdf, last accessed on March 27, 2017.
- [27] S.P. Malace, B.D. Sawatzky and H. Gao, "Studies of single-photoelectron response and of performance in magnetic field of a H8500C-03 photomultiplier tube", Journal of Instrumentation **8** (2013), P09004.
- [28] H. Voskanyan, W. Phelps, private communication.
- [29] A. Golubev, "Exponentially modified Gaussian (EMG) relevance to distributions related to cell proliferation and differentiation", Journal of Theoretical Biology **262** (2) (2010), p.257. See also http://en.wikipedia.org/wiki/Exponentially_modified_Gaussian_distribution, last accessed on March 27, 2017.
- [30] V. Kubarovsky, A. Kim, to be published.